Reproducible 3D printed head tanks for electrical impedance tomography with realistic shape and conductivity distribution

2017 Physiol. Meas. 38 1116

(http://iopscience.iop.org/0967-3334/38/6/1116)

OPEN ACCESS
IOP Publishing | Institute of Physics and Engineering in Medicine Physiological Measurement
Physiol. Meas. **38** (2017) 1116–1131 https://doi.org/10.1088/1361-6579/aa6586

Reproducible 3D printed head tanks for electrical impedance tomography with realistic shape and conductivity distribution

James Avery[1], **Kirill Aristovich, Barney Low and David Holder**

University College London, London WC1E 6BT, United Kingdom

E-mail: j.avery@ucl.ac.uk

Received 11 January 2017, revised 16 February 2017
Accepted for publication 9 March 2017
Published 22 May 2017

Abstract

Objective. Electrical impedance tomography (EIT) has many promising applications in brain injury monitoring. To evaluate both instrumentation and reconstruction algorithms, experiments are first performed in head tanks. Existing methods, whilst accurate, produce a discontinuous conductivity, and are often made by hand, making it hard for other researchers to replicate. *Approach.* We have developed a method for constructing head tanks directly in a 3D printer. Conductivity was controlled through perforations in the skull surface, which allow for saline to pass through. Varying the diameter of the holes allowed for the conductivity to be controlled with 3% error for the target conductivity range. Taking CT and MRI segmentations as a basis, this method was employed to create an adult tank with a continuous conductivity distribution, and a neonatal tank with fontanelles. *Main results.* Using 3D scanning a geometric accuracy of 0.21 mm was recorded, equal to that of the precision of the 3D printer used. Differences of 6.1% $\pm$ 6.4% ($n = 11$ in 4 tanks) compared to simulations were recorded in c. 800 boundary voltages. This may be attributed to the morphology of the skulls increasing tortuosity effects and hole misalignment. Despite significant differences in errors between three repetitions of the neonatal tank, images of a realistic perturbation could still be reconstructed with different tanks used for the baseline and perturbation datasets. *Significance.* These phantoms can be reproduced by any researcher with access to a 'hobbyist' 3D printer in a

[1] Author to whom any correspondence should be addressed.

matter of days. All design files have been released using an open source license to encourage reproduction and modification.

Keywords: electrical impedance tomography (EIT), phantom, head tank, rapid prototyping, 3D printing, realistic shape

(Some figures may appear in colour only in the online journal)

1. Introduction

Electrical impedance tomography (EIT) is a medical imaging technique which produces images of the internal electrical impedance of a subject from multiple measurements using surface electrodes. EIT of the brain has many potential applications including stroke type differentiation (Romsauerova *et al* 2006), localising epilepsy (Fabrizi *et al* 2006), and monitoring brain injuries such as intracranial and intraventricular haemorrhage, cerebral oedema, and ischaemia (Tang and Sadleir 2011, Dai *et al* 2013, Manwaring *et al* 2013, Fu *et al* 2014).

Studies in phantoms represent a bridge between idealised computer simulations and clinical measurements in which instrumentation noise is present but errors in modelling the electric fields are minimised. Constructing a representative head phantom poses a particular challenge, given the irregular geometry of the head and the complexity of the internal tissues. The conductivity of the skull is inhomogeneous due to variations in the layered structure throughout (Law 1993, Akhtari *et al* 2002). These layers result in a low, spatially variable conductivity, which is highly anisotropic, with tangential:normal conductivity ratios of 10:1 when modelled as a homogenous layer (Wolters *et al* 2006) or 1.4:1 when considered as three separate layers (Sadleir and Argibay 2007).

Previously, these complexities have necessitated considerable simplifications when creating phantoms for EIT. Cylindrical, hemispherical and spherical tanks are common as they are quick to achieve and do not require finite element models (FEMs) as geometrically detailed as those of the cranial cavity (Liston *et al* 2004, Tang *et al* 2010, Ahn *et al* 2011, Sperandio *et al* 2012). To improve upon these models, a more realistic tank incorporating a real skull was created by Tidswell *et al* (2003). Subsequently, the prevalence of rapid prototyping technology has enabled phantoms to replicate the morphology of the head with a high precision, either by 3D printing the tanks directly (Tang and Sadleir 2011), or more commonly, printing moulds used for casting (Collier *et al* 2012, Li *et al* 2014, Mobashsher and Abbosh 2014).

Creating a volume conductor model of the skull mimicking the spatial variation of the electrical properties has yet to be achieved in the literature. Layers of carefully chosen concentrations of saline, gel or plaster of paris have been used to create a single shell of accurate, but spatially invariant conductivity (Liston *et al* 2004, Collier *et al* 2012, Sperandio *et al* 2012). To address this invariance, Li *et al* (2014) created a geometrically accurate phantom with eight separate bone structures, each with a different, but fixed conductivity. Tidswell *et al* (2003) incorporated a real skull in their phantom, which may have replicated the spatial variability of the skull structure, the dead tissue was not representative of the conductivity itself. There has been less focus in the literature on phantoms in neonatal head EIT; the most detailed phantom to date, was geometrically representative but did not include the skull (Tang and Sadleir 2011).

As well as lacking the true smooth spatial distribution of the skull, these phantoms also have practical disadvantages. The agar or gypsum used in the skull shells degrades over time in contact with air or water, making them unsuitable for sporadic use over the long term. At least some elements are also constructed by hand, which makes them difficult for other

researchers to replicate. Further, even small changes in boundary shape can result in significant modelling errors (Nissinen *et al* 2010), so results may not be repeatable even in cases where the method is sufficiently described.

The purpose of this study was to develop a method of creating head tanks for EIT which are readily reproducible, whilst allowing for smoothly varying conductivity across the skull. It employed rapid prototyping and extruded plastic to create both the tank and skull directly, for both and adult and neonatal head. Perforations were made in the skulls in order to simulate their realistic conductivities. This approach reduces the variation during construction and thus offers practical advantages to any research group wishing to utilise reproducible faithful tanks for EIT evaluation.

As the tanks were constructed entirely with insulating plastic, a method of controlling the conductivity through surface perforations was first validated in small tubular tanks. Using CT and MRI segmentations as reference, both a neonatal and adult tank were constructed with the method developed herein. To assess the accuracy of the construction, the adult tank was compared to the ideal CAD model using high resolution optical 3D scanning. Simulations of the voltages expected when using the same CAD model were then compared to those obtained experimentally. Finally, the repeatability of the method was evaluated in three neonatal phantoms, comparing the experimental voltages and reconstructed images in each case.

2. Materials and methods

2.1. Modelling conductivity

To maximise the reproducibility of the phantom, the entirety of tank and skull, with the exception of the electrodes themselves, were constructed directly by the 3D printer. This precluded methods commonly used to create multi shell phantoms, namely casting plaster of paris (Liston *et al* 2004, Li *et al* 2014) or agar and volume conductive film (Sperandio *et al* 2012). The technique employed in these tanks was of a solid printable skull with variable diameter surface perforations, which allow saline, and thus current, to pass through. The effective resistivity can be approximated through a simple estimation of the area ratio of saline to insulating plastic, equation (1). By smoothly altering the density or diameter of the holes the effective conductivity can vary smoothly across the phantom, as opposed to a fixed value per segment

$$\rho_{\text{eff}} \approx \frac{A_{\text{total}}}{A_{\text{saline}}}\rho_{\text{saline}}. \tag{1}$$

To validate this model experimentally, a square tube phantom with two electrodes was created, figure 1(a), between which grids of differing hole density and diameter could be inserted. The tank was filled with 0.2% saline, and the three components formed a water tight seal. Inserts with hole spacing of 5, 6 and 8 mm were created with hole diameters 1–3 mm in 0.5 mm increments, covering the range which could reliably be 3D printed. The impedance was measured with a Hewlett-Packard HP4284A impedance analyser at 1 kHz. Corrections for the electrode contact impedance were calculated using measurements with three different tank lengths and with no insert present.

The theoretical effective resistance was calculated for the cross sectional surface area equivalent to that occupied by the combined aperture cross sectional area A_{saline}, figure 1(b). In the tank, the target resistivity could only be matched with $<3\%$ error using a hole spacing of 5 mm and diameters between >1 mm and <2.5 mm, equivalent to a ratio of A_{saline} between 0.05 and 0.13. This was likely because diameters outside this range were not accurately reproduced by

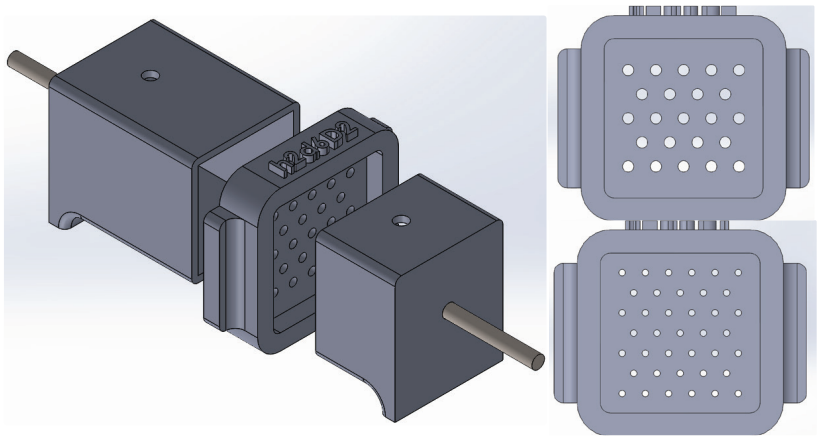

(a)

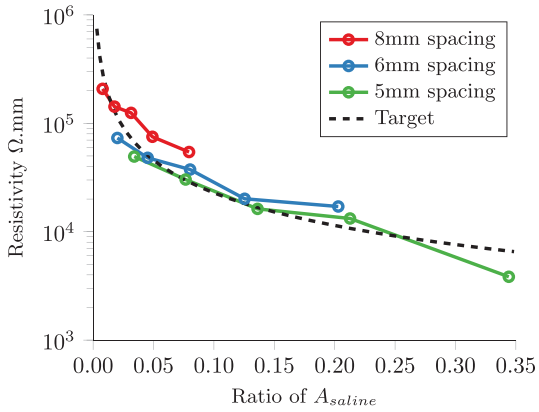

(b)

Figure 1. (a) Left: tubular phantom with two sections of varying length and resistive surface inserts, right: 2 mm holes with 6 mm spacing and 1 mm with 5 mm spacing (b) relationship between effective resistivity ρ_{eff} and combined cross sectional area of surface perforations, A_{saline} for three different hole spacing.

the 3D printer, resulting in errors >20%. Therefore, in subsequent phantom designs, a hole spacing of 5 mm was used and diameters adjusted to stay within this range.

2.2. Tank design

The geometry for the phantoms was obtained from segmentations of a combination of CT and MRI for the adult head, and a CT for the neonatal head. The resolution of these scans were <1 mm in all 3 dimensions, providing sufficient resolution to obtain segmentations of the scalp, skull, dura, grey and white matter and CSF in the MRI (Jehl *et al* 2014), and the scalp and skull in the CT. Smoothing of segmentation artefacts was first performed in MeshLab (Cignoni *et al* 2008) before trimming of extraneous features and further artefact removal in FreeCAD (www.freecadweb.org/). This smoothed geometry could then be converted to the solid parametric format traditionally used in CAD, figure 2.

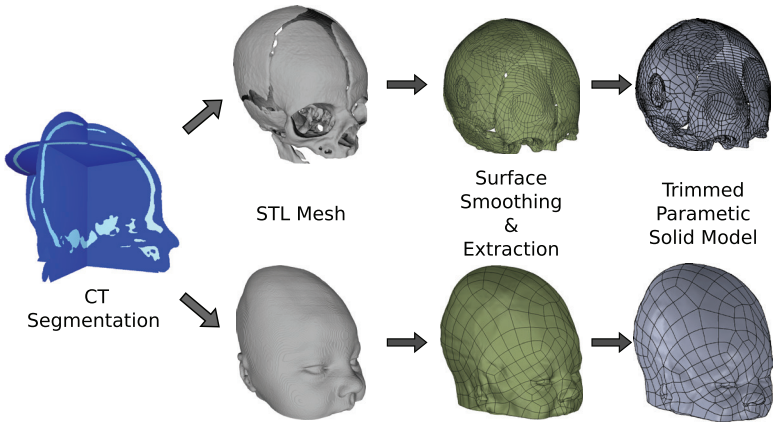

Figure 2. Workflow to create solid models from a CT segmentation for the design of the neonatal tank.

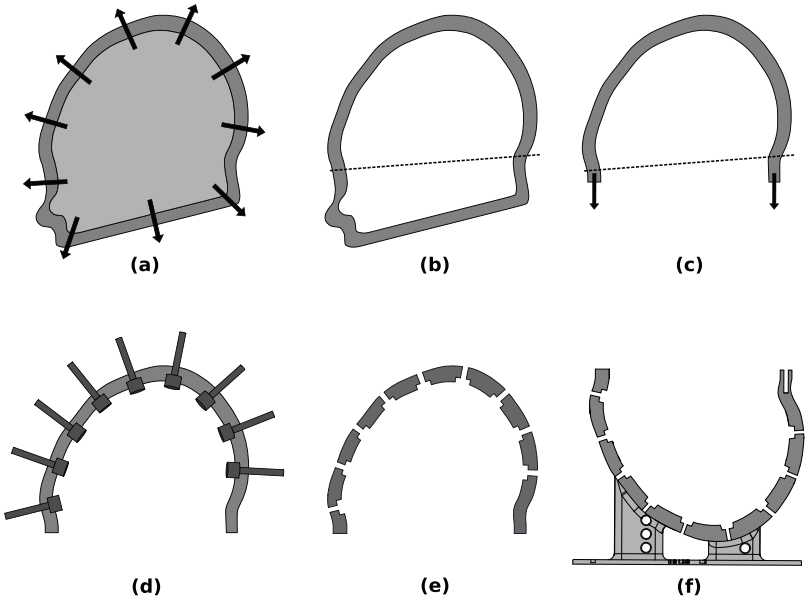

Figure 3. Design of tank models. (a) scalp duplicated and scaled by 10% to create the outer tank surface, (b) inner surface removed and shell split below inion-nasion line, (c) the model was trimmed and the walls extended 10 mm, (d) electrodes with clearance were arranged in modified EEG 10–20 positions, (e) the clearance electrodes removed from the tank volume, (f) supports added and model was finalised.

To create the tanks, figure 3, the models were split along a plane parallel to that described by the inion-nasion line, the offset chosen to include the entirety of the brain cavity yet remove as much of the neck and facial structures as possible. This is a common simplification in brain EIT, as structures like the ear canal and eyeballs are challenging to model even in simulation, and their effect on EIT measurements still require investigation (Vauhkonen *et al* 1999, Tidswell *et al* 2003, Liston *et al* 2004, Sperandio *et al* 2012, Li *et al* 2014). This plane also

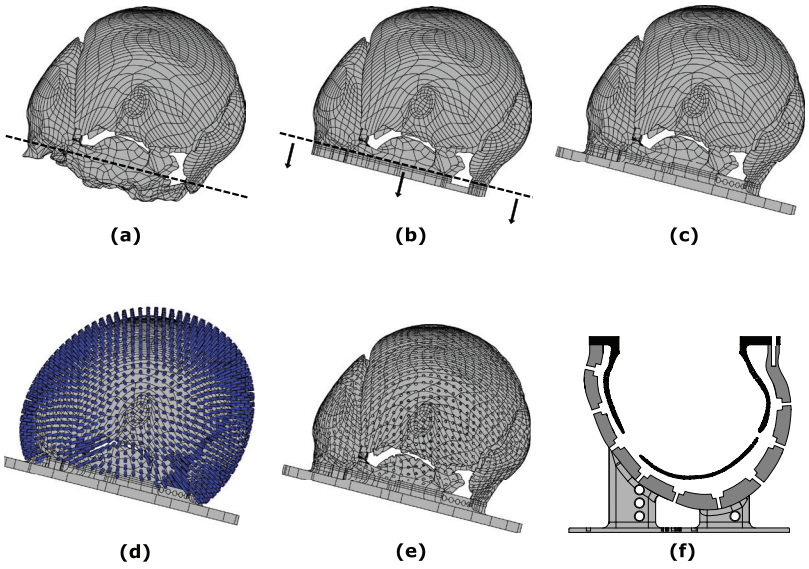

Figure 4. Design of skull models. (a) skull model was split along the same plane as figure 3, (b) the model was trimmed and walls vertically extended 1 cm to match those of the tank, (c) a support base added to position the skull in the tank, (d) cylinders were created normal to the surface, centred at evenly distributed points 5 mm apart, (e) the cylinders were subtracted from the tank volume giving the final model, (f) skull then suspended in the tank.

defines the height of the saline within the tank, and thus the extent of the volume used for mesh generation.

In both tanks, 32 electrodes and a ground electrode were positioned based on the distributions proposed by Tidswell *et al* (2001b), which includes 21 positions from the EEG 10–20 system (Jasper 1958), six from the extended 20–20 and four additional positions. These additional positions were modified in these tanks to the nearest locations in either the 10–10 or 10–5 extensions (Oostenveld and Praamstra 2001). Recesses were then created at each of these points to ensure that when placed, the electrodes were flush against the tank walls. To create these recesses, models of the electrodes expanded by 0.2 mm were aligned normal to the surface at each of these locations and then subtracted from the tank volume. To complete the models, support legs and a base were then added.

2.3. Skull design with realistic conductivity distribution

To create the skull phantoms, the model was cut along the same plane parallel to the inion—nasion line, figure 4, leaving only the bone encasing the brain and the resultant surfaces were extended to match the height of the tank walls. Support structures were added so the skull could be suspended in place inside the tank, aligned through corresponding concentric holes in both pieces. In the neonatal tank, it was necessary to split the skull into two parts along the lambdoid suture between the parietal and occipital bones. Each half was then positioned separately inside the tank, forming a water tight seal once correctly aligned.

2.3.1. Conductivity distributions. The conductivity for the adult skull was based upon the results from Tang *et al* (2008) at 1kHz, and spatial distribution obtained from Li *et al* (2014). Given the resolution of the 3D printer and the surface perforation method, the sutures between bone types were neglected.

The sphenoid and temporal bones at the side of the head are of the same 'quasi-compact' bone type, $\sigma = 0.005\,\mathrm{S\,m^{-1}}$. The frontal and occipital bones at the front and back of the head are both 'standard tri-layer', with $\sigma = 0.0126\,\mathrm{S\,m^{-1}}$. The conductivity at the top of the head—the parietal bone, is of the 'quasi-tri-layer' type, $\sigma = 0.0069\,\mathrm{S\,m^{-1}}$ (Tang *et al* 2008). Thus, starting from the top of the head, the conductivity increases by 87% towards the front and back of the head, and decreases by 32% towards the sides. Taking the top of the skull as the origin with $\sigma_0 = 0.0069\,\mathrm{S\,m^{-1}}$, the conductivity was modelled as a linear combination of an increase towards the front and back (x direction) of the skull and a decrease in conductivity towards the sides (y direction), equation (2)

$$\sigma_{xy} = \sigma_0\left(1 + 0.87\frac{x}{x_{\max}} - 0.32\frac{y}{y_{\max}}\right). \tag{2}$$

As the spatial distribution is not as well understood in the literature, the conductivity for the neonatal skull phantom was fixed at a value of $0.03\,\mathrm{S\,m^{-1}}$ as suggested by Pant *et al* (2011).

2.3.2. Spatially varying conductivity phantoms. The holes were positioned on the surface of the skulls in an evenly spaced 5 mm distribution. The diameter of each hole was then calculated based upon a combination of equations (1) and (2), assuming 0.2% saline concentration. Cylinders of the required diameter, aligned to the normal of the surface were generated at each point. The cylinders were then removed from the skull model using the same Boolean subtraction to create the electrode recesses.

2.4. Construction

The phantoms were created from polylactic acid (PLA) using a MakerBot Replicator 2 Desktop 3D printer (MakerBot, Brooklyn, NY), a common 'hobbyist' fused deposition modelling (FDM) 3D printer. The rated accuracy of the printer is 0.1 mm in the X and Y dimensions and user controlled within a range of 0.1–0.4 mm in the Z direction. All models were printed entirely solid to ensure they are water tight, the Z layer height was set to 0.2 mm to reduce the build time to less than 48 h. Support material artefacts and burrs were removed through sanding and blasting with compressed air. The electrodes were 316 stainless steel, chosen for its high corrosion resistance, and sealed in place with silicon adhesive.

2.5. Geometry testing—deviation analysis

Determining the accuracy of the resultant geometry is made difficult by the irregular morphology of the head. Previous techniques compare distances between key points on the tank measured by hand. The error is then expressed as a percentage of the distance in either the initial CT (Silva *et al* 2008) or a cast used in a previous manufacturing step (Li *et al* 2014). In these cases, mean errors ranging from 0.6 mm or 0.75% to 1.07 mm or 2.67% have been found.

These methods have two drawbacks: measurements are not compared to the same model used in simulations and they do not adequately capture the spatial distribution of the error across the head. The method proposed in this study is 'deviation analysis', a common reverse-engineering technique (Várady *et al* 1997), wherein surfaces of the CAD model are compared point-by-point to those obtained through a high-precision scan. The adult tank was

scanned using a Creaform Go!Scan20 3D optical scanner (Creaform Inc. Québec, Canada), to provide a mesh of the surface, with an accuracy of $\leqslant$0.2 mm and $>$2 million elements. Scanning targets were placed upon the model to enable registration and alignment with the CAD model. To simplify the scanning procedure, only the inner surface of the tank was considered, and the electrodes were removed from the analysis due to artefacts arising from the reflective surfaces.

2.6. Comparison to EIT simulations

2.6.1. Data collection. Data were collected in both tanks using the UCL 'ScouseTom' EIT system (Avery *et al* 2017). For the adult tank experiments, the injection electrode protocol proposed by Malone *et al* (2014) was used, with 31 injection pairs chosen to maximise the number of independent measurements. A protocol with 32 injections was used for the neonatal tank measurements, which maximised the number of injections from opposites sides of the head. In all experiments, the current injected was 200 μA amplitude at 1.4 kHz, with 75 ms per injection pair and results averaged over 20 complete frames. The tanks were filled with 0.2% saline with a conductivity of 0.4 S m^{-1}, to represent the scalp. Experiments were performed first without the skull present, and then with the skull in place.

2.6.2. Data analysis. The boundary voltages collected in each experiment were compared to simulations in $\approx$4 million element FEMs generated from the CAD models using the parallel EIT solver (PEITS) (Jehl *et al* 2014). The error was calculated as the absolute difference between the experimental and simulated voltages for each measurement. The data were summarised both as a mean and standard deviation in absolute voltage and as a percentage of the simulated voltage. Measurement channels with a simulated voltage less than 0.1 mV were removed from this analysis, based on the threshold described by Packham *et al* (2012), to avoid overestimation of the error from noise on small channels. The results were thus expressed as a mean plus standard deviation calculated on 819 and 775 voltage measurements for the adult and neonatal tanks respectively. Results below, unless stated otherwise, were expressed as mean and standard deviation.

2.7. Reproducibility of method

Alongside the first neonatal tank, labelled 'tank 1', two further neonatal tanks and skulls were constructed, labelled tank 2 and 3, and the data collection procedure repeated in each one. To represent the expected intermittent usage of the tanks, each dataset was collected starting from an empty tank with the EIT system disconnected each time. These voltages were analysed using the same methods as the previous experiments.

EIT images were reconstructed of the conductivity changes resulting from the insertion of a 20 mm diameter sponge of approximately 10% contrast located in the anterior position. Similar perturbations have been used previously to represent the change expected resulting from cell swelling in epilepsy (Tidswell *et al* 2001b, Fabrizi *et al* 2009). The perturbation dataset was collected in tank 1 only, with the baseline from all three tanks used as a reference for three separate images. Reconstructions were performed using the method described by Aristovich *et al* (2014), using Zeroth order Tikhonov regularisation with noise based correction and hexahedral meshes of c. 100 000 elements.

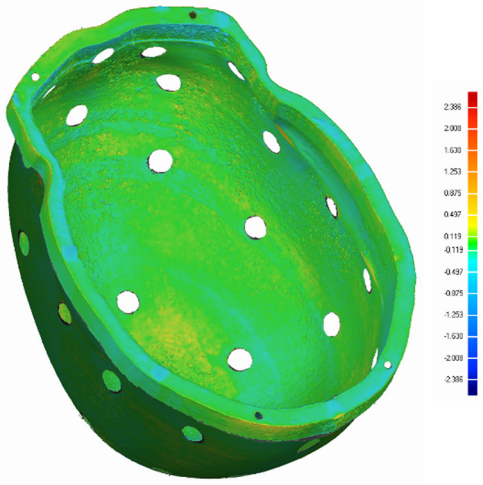

Figure 5. Deviation analysis comparing 3D scan of adult tank to target CAD model.

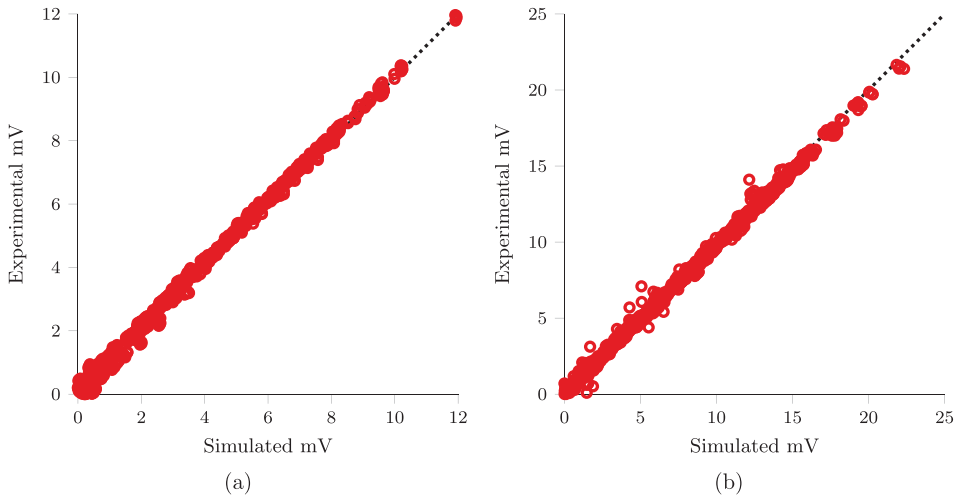

Figure 6. Comparison of voltages (a) in adult head tank $R^2 = 0.997$ and (b) in adult head tank with skull $R^2 = 0.997$.

3. Results

3.1. Geometry analysis

The deviation in the adult tank was 0.21 mm $\pm$ 0.101 mm. The error was distributed evenly across the tank, figure 5, with the exception of occasional printing artefacts at the rim of tank and at the bottom of tank, equivalent to the top of the head.

3.2. Comparison to simulation

3.2.1. Adult tank. Qualitatively, the simulated and experimental voltages in the adult tank were in good agreement, figure 6(a), with a correlation coefficient of $R^2 = 0.997$. The error

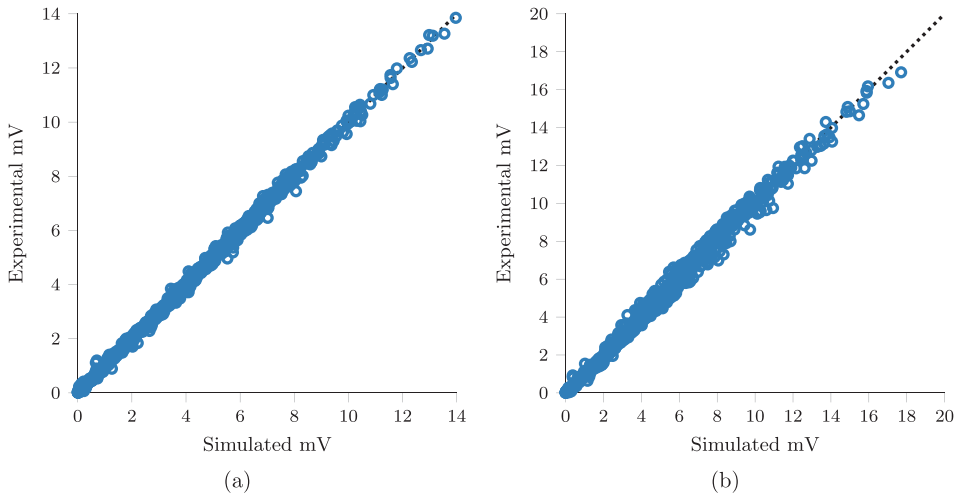

Figure 7. Comparison of voltages (a) in neonatal head tank $R^2 = 0.999$ and (b) in neonate head tank with skull $R^2 = 0.994$.

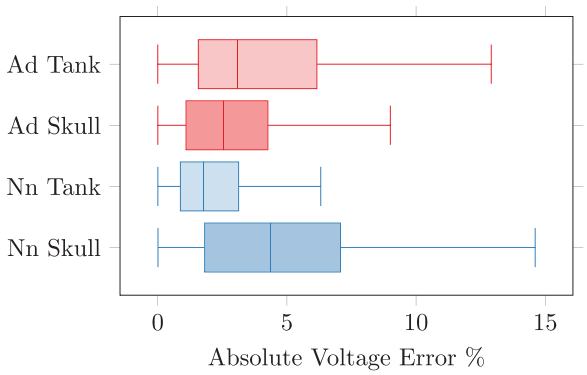

Figure 8. Absolute percentage errors in voltages compared to simulation for both adult (Ad) and neonatal (Nn) tanks with and without skull.

across all measurements was 0.147 ± 0.099 mV. Injecting between electrode positions FP1 and P04 produced the greatest error of 0.251 mV.

3.2.2. Adult tank with skull. The inclusion of the skull had no effect upon the correlation between the simulated and experimental voltages $R^2 = 0.997$, figure 6(b). However, the overall error increased to 0.215 ± 0.229 mV, and some channels had significantly larger errors than the average. These were all found either when injecting between FP2 and 0Z, or measuring at T4, with a mean error of 0.513 and 0.439 mV respectively.

3.2.3. Neonatal tank. In the neonatal tank, figure 7(a), the simulated and experimental voltages, were also in good correlation $R^2 = 0.999$, with an error of 0.079 ± 0.062 mV. The largest errors were found when injecting current between the electrodes at TP8 and AF3, with an error of 0.187 mV.

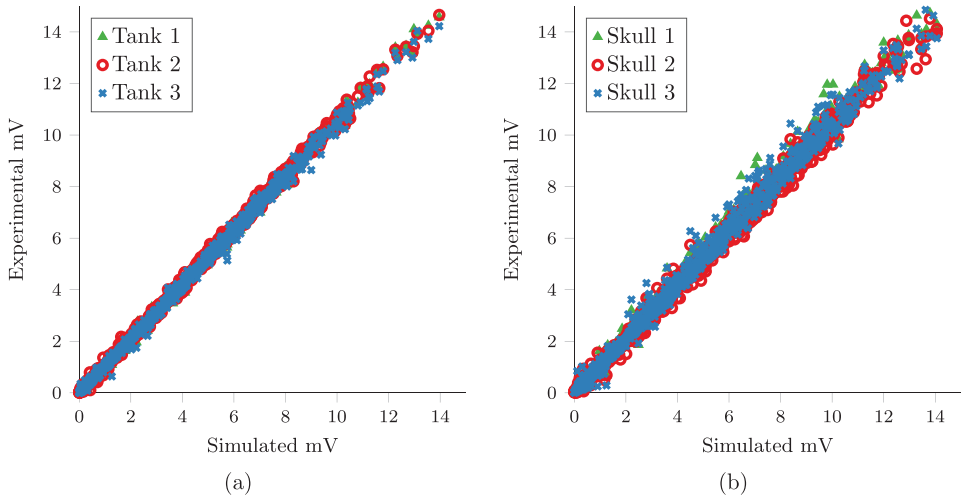

Figure 9. Comparison of voltages recorded in (a) three separate neonatal tanks, and (b) three separate neonatal tanks with skull, averaged over three repeats each.

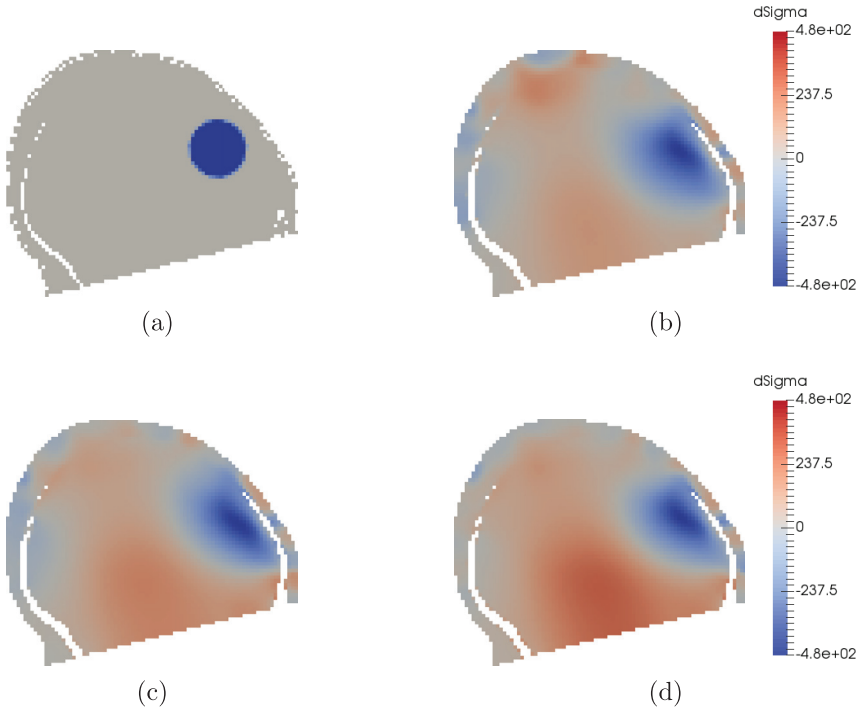

Figure 10. Perturbation of 10% contrast (a) ideal location, recorded in phantom 1 reconstructed with (b) phantom 1 as baseline (c) phantom 2 as baseline (d) phantom 3 as baseline.

3.2.4. Neonatal tank with skull. The addition of the skull decreased the correlation with the simulated voltages, figure 7(b), to $R^2 = 0.994$. This was also reflected in the increased error of 0.185 ± 0.198 mV. The largest errors were found when injecting between AF8 and FCz, with an error of 0.569 mV.

3.2.5. Summary. The mean error expressed as a percentage, figure 8, in the adult tank was 4.87% without the skull and 4.50% including the skull. The error in the neonatal tank was 2.4% and 5.14% for measurements without and with the skull respectively. In both cases the inclusion of the skull significantly changed the mean error $P < 0.05$, decreasing by 0.37% for the adult tank, and increasing error by 1.74% for the neonatal tank.

3.3. Reproducibility

The recorded voltages for all three neonatal tanks were consistent, figure 9(a), with $R^2 = 0.999$, $R^2 = 0.998$ and $R^2 = 0.998$. The mean error across all measurements and repeats was significantly less for tank 3 $P < 0.05$, with 5.06% compared to 6.2 and 6.3% for tanks 1 and 2 respectively. As is clear from figure 9(b), the error with three different skulls was both less correlated with simulation $R^2 = 0.994$, $R^2 = 0.995$ and $R^2 = 0.993$ respectively, and the measurements with largest errors were different for each phantom. The skull phantom in tank 2 had a mean error of 5.3% which was significantly less $P < 0.05$ than the 7.63% error in tank 1 and 7.1% error in tank 3.

Despite these differences in baseline voltages between the phantoms, the perturbation was successfully reconstructed in every case, including both mismatched datasets, figure 10. The distance between ideal and reconstructed centre of mass for the matched datasets, figure 10(b), was 2.9 mm or 2.6% of the tank width. This increased to 3.2 and 3.4 mm or 2.9 and 3.0% when tank 2 and tank 3 were used as baseline recordings respectively. There were also increased artefactual positive changes and distortion in the shape of the reconstructed perturbations with mismatched phantoms.

4. Discussion

Using 3D scanning allowed for direct comparison with the mesh used in EIT reconstructions, and overcame the limitations of methods implemented previously in the literature. A consistent error of 0.21 mm was found across the tank, which is close to the rated accuracy of both the 3D printer and 3D scanner used. Printing artefacts were largely confined to areas which would not affect the experimental results; however some were still present at the top of the head. Thus the accuracy could be improved through the use of a more accurate rapid prototyping technology, and better post processing methods. Despite these, the mean error is similar to that found using distances measured by hand (Silva *et al* 2008, Li *et al* 2014).

The accuracy of the method is further demonstrated in the comparison of simulated and experimental voltages, which are all in clear agreement ($R^2 > 0.994$) for all injections and measurements. Without the skull, the measurements with greatest error occur at electrodes with the greatest surface curvature, where the electrodes may not be perfectly aligned with, or flush against, the tank wall. These effects were less pronounced in the neonatal tank and as such had reduced error, both as a voltage and as a percentage: 0.079 mV and 2.4% compared to 0.147 mV and 4.87%. The larger percentage errors, >8%, all correspond to the channels with the lowest boundary voltages <1 mV, and are thus more susceptible to measurement noise and modelling errors. This explains why counter-intuitively, the mean error decreased

in the adult tank with the inclusion of the skull, from 4.87% to 4.5%, whilst the voltage error increased from 0.147 mV to 0.215 mV. The inclusion of the skull approximately doubled the mean voltage, resulting in fewer low standing potential, high error channels. This was not the case for the neonatal tank, in which the error doubled both as an absolute voltage from 0.079 mV to 0.185 mV, and as a percentage, from 2.4% to 5.14%.

In both tanks the errors were greatest when injecting current from opposite sides of the head, from the anterior to the posterior electrodes. In both tanks, this corresponds to the areas with the greatest curvature. In which case, the normals of the skull and nearby scalp surfaces may not be aligned, increasing the errors arising from tortuosity effects. This is especially true of the parts of the orbital plate included in the neonatal tank, which in some cases is perpendicular to the nearest tank surface. Given the anisotropy of the conductivity using surface perforations, the approximation only holds when the holes are aligned with the injecting electrodes. Defining the axis of the holes in the skull perpendicular to the nearest scalp surface as opposed to the skull could reduce this error. Further, the electrodes with the greatest error are also closest to the top of the tank, and are thus more vulnerable to changes in saline level between experiments.

Assessment of the tanks with respect to the literature is difficult as the error is often not quantified to the same extent as in this study. The most detailed study using plaster of paris showed there was no statistical difference with conductivity distributions in the skull, and the error in transimpedance, while not quantified by the authors, appears to be 1–5% in six measurements (Li *et al* 2014). This is approximately the interquartile range of the errors in the adult skull measurements in figure 8, suggesting the errors are similar in the two tanks. The error across all recordings in all tanks was 6.1% $\pm$ 6.4% ($n = 11$ in 4 tanks). The reconstructions in figure 10 suggest the effect of these modelling errors is likely minimised when subtracting the reference dataset in time difference imaging. Absolute or multi-frequency imaging, without this subtraction, are much more sensitive to these modelling errors, but the acceptable range is not yet quantified in the literature. However, a study in a similar adult head tank demonstrated that these errors are large enough to mask any real conductivity changes (Jehl *et al* 2015).

The significant differences in the errors between repetitions of the tank are likely to be caused by printing artefacts. It was not always possible to fully remove the support material from the electrode recesses in the tank, leading to slight misalignment of electrodes when they were inserted. Similarly, printing the required number of small diameter holes in thin shells was on the limits of what was capable with the printer. Consequently, the diameter of all c. 3000 holes did not meet the rated accuracy in every instance. As with the geometric accuracy, both of these issues would be improved through the use of a higher resolution rapid prototyping technology.

The results show that creating a head tank directly via rapid prototyping yields a phantom that is both quick to build—with our setup, both tanks could be completed within a week—and provides stable results over time and between copies. However, given the material is purely insulating, replicating the conductivity of the skull is not without compromise. The conductivity of the skull phantom is highly anisotropic, as it is close to a pure insulator in the tangential direction. This is a less realistic representation of the true conductivity than the isotropic layers used in existing methods. In both current injection protocols chosen, the direction of injected current was normal to the skull surface, where errors arising from this anisotropy are minimised. It is likely that if an ‘adjacent pair’ or similar protocol was chosen, the error would increase. As the whole tank is filled with a single saline concentration, the scalp and brain volumes have the same conductivity. Whilst this a common simplification (Tidswell *et al* 2001a, Li *et al* 2014), it does not reflect the true tissue properties. Further, each of the skulls were calculated based upon empirical values from the literature at 1 kHz (Tang *et al* 2008, Pant *et al* 2011), and thus experiments at higher frequencies would benefit from

recalculation. In this case, multi-frequency studies over a wide frequency range could require a multitude of different skulls, which increases the chances of errors arising from printing artefacts or misalignment. Finally, the spatial variation of the adult skull conductivity is currently too simplified to represent the true distribution. Skull conductivity has been shown to correlate with ratio of diploe thickness (Tang *et al* 2008). Segmentation of the diploe layer could thus be used to estimate a per element conductivity in the FEM, and the hole diameter recalculated using these values.

5. Conclusion

Previous head tanks utilised rapid prototyping to create moulds for casting conductive materials. Whilst this may enable accurate representation of the geometry of the head tissues, this indirect use does not take full advantage of reproducibility of the technology. In this study, a novel construction method was described wherein the tank and skull are constructed entirely by 3D printing, and the effective skull conductivity is controlled through surface perforations. This technique was shown to have an error of approximately 3% across the target conductivity range in test phantoms. Two phantoms were created: an adult tank with a smoothly varying skull conductivity, and a neonatal tank with fontanelles. 3D scanning measured a geometric error of 0.21 mm, equal to the rated accuracy of the 3D printer used. Curvature and tortuosity effects increased the error to ≈5% in the full tank models. Despite significantly different errors in three neonatal tanks, reconstructions of biologically representative perturbations were successful with mismatched reference and perturbation datasets.

These phantoms can be replicated by any researcher with access to a 'hobbyist' standard 3D printer, with minimal construction by hand. The models and software to create these tanks have been released on an open-source license (see appendix), to encourage reproduction and modification.

Acknowledgment

The authors would like to acknowledge Mrs Tugba Demiray who collaborated on earlier designs of the adult and tubular phantoms. These were then superseded by those constructed for the experiments detailed in this manuscript. This work was supported by EPSRC grant EP/M506448/1.

Appendix. Hardware and software resources

All CAD models and software used in creating both tanks are available at https://github.com/EIT-team/Tanks, released under a GNU General Public License v3.0. Replication, contributions and distribution are welcomed.

References

Ahn S, Oh T I, Jun S C, Seo J K and Woo E J 2011 Validation of weighted frequency-difference EIT using a three-dimensional hemisphere model and phantom *Physiol. Meas.* **32** 1663–80

Akhtari M *et al* 2002 Conductivities of three-layer live human skull *Brain Topogr.* **14** 151–67

Aristovich K Y, dos Santos G S, Packham B C and Holder D S 2014 A method for reconstructing tomographic images of evoked neural activity with electrical impedance tomography using intracranial planar arrays *Physiol. Meas.* **35** 1095–109

Avery J, Dowrick T, Faulkner M, Goren N and Holder D 2017 A versatile and reproducible multi-frequency electrical impedance tomography system *Sensors* **17** 280

Cignoni P, Callieri M, Corsini M, Dellepiane M, Ganovelli F and Ranzuglia G 2008 MeshLab: an open-source mesh processing tool *6th Eurographics Italian Chapter Conf.* pp 129–36

Collier T J, Kynor D B, Bieszczad J, Audette W E, Kobylarz E J and Diamond S G 2012 Creation of a human head phantom for testing of electroencephalography equipment and techniques *IEEE Trans. Bio-Med. Eng.* **59** 2628–34

Dai M, Li B, Hu S, Xu C, Yang B, Li J, Fu F, Fei Z and Dong X 2013 *In vivo* imaging of twist drill drainage for subdural hematoma: a clinical feasibility study on electrical impedance tomography for measuring intracranial bleeding in humans *PloS One* **8** e55020

Fabrizi L, McEwan A, Oh T, Woo E J and Holder D S 2009 A comparison of two EIT systems suitable for imaging impedance changes in epilepsy *Physiol. Meas.* **30** S103–20

Fabrizi L, Sparkes M, Horesh L, Perez-Juste Abascal J F, McEwan A, Bayford R H, Elwes R, Binnie C D and Holder D S 2006 Factors limiting the application of electrical impedance tomography for identification of regional conductivity changes using scalp electrodes during epileptic seizures in humans *Physiol. Meas.* **27** S163–74

Fu F *et al* 2014 Use of electrical impedance tomography to monitor regional cerebral edema during clinical dehydration treatment *PloS One* **9** e113202

Jasper H H 1958 Report of the committee on methods of clinical examination in electroencephalography *Electroencephalogr. Clin. Neurophysiol. Suppl.* **10** 370–5

Jehl M, Avery J, Malone E, Holder D and Betcke T 2015 Correcting electrode modelling errors in EIT on realistic 3D head models *Physiol. Meas.* **36** 2423–42

Jehl M, Dedner A, Betcke T, Aristovich K, Klofkorn R and Holder D 2014 A fast parallel solver for the forward problem in electrical impedance tomography *IEEE Trans. Bio-Med. Eng.* **9294** 1–13

Law S K 1993 Thickness and resistivity variations over the upper surface of the human skull *Brain Topogr.* **6** 99–109

Li J B *et al* 2014 A new head phantom with realistic shape and spatially varying skull resistivity distribution *IEEE Trans. Bio-Med. Eng.* **61** 254–63

Liston A D, Bayford R H and Holder D S 2004 The effect of layers in imaging brain function using electrical impedance tomograghy *Physiol. Meas.* **25** 143–58

Malone E, Jehl M, Arridge S, Betcke T and Holder D 2014 Stroke type differentiation using spectrally constrained multifrequency EIT: evaluation of feasibility in a realistic head model *Physiol. Meas.* **35** 1051–66

Manwaring P K, Moodie K L, Hartov A, Manwaring K H and Halter R J 2013 Intracranial electrical impedance tomography: a method of continuous monitoring in an animal model of head trauma *Anesthesia Analgesia* **117** 866–75

Mobashsher A T and Abbosh A M 2014 Three-dimensional human head phantom with realistic electrical properties and anatomy *IEEE Antennas Wireless Propag. Lett.* **13** 1401–4

Nissinen A, Kolehmainen V and Kaipio J P 2010 Compensation of errors due to incorrect model geometry in electrical impedance tomography *J. Phys.: Conf. Ser.* **224** 012050

Oostenveld R and Praamstra P 2001 The five percent electrode system for high-resolution EEG and ERP measurements *Clin. Neurophysiol.* **112** 713–9

Packham B, Koo H, Romsauerova A, Ahn S, McEwan A, Jun S and Holder D 2012 Comparison of frequency difference reconstruction algorithms for the detection of acute stroke using EIT in a realistic head-shaped tank *Physiol. Meas.* **33** 767–86

Pant S, Te T, Tucker A and Sadleir R R J 2011 The conductivity of neonatal piglet skulls *Physiol. Meas.* **32** 1275–83

Romsauerova A, McEwan A, Horesh L, Yerworth R, Bayford R H and Holder D S 2006 Multi-frequency electrical impedance tomography (EIT) of the adult human head: initial findings in brain tumours, arteriovenous malformations and chronic stroke, development of an analysis method and calibration *Physiol. Meas.* **27** S147

Sadleir R and Argibay A 2007 Modeling skull electrical properties *Ann. Biomed. Eng.* **35** 1699–712

Silva D N, Gerhardt de Oliveira M, Meurer E, Meurer M I, Lopes da Silva J V and Santa-Bárbara A 2008 Dimensional error in selective laser sintering and 3D-printing of models for craniomaxillary anatomy reconstruction *J. Cranio-Maxillo-Facial Surg.* **36** 443–9

Sperandio M, Guermandi M and Guerrieri R 2012 A four-shell diffusion phantom of the head for electrical impedance tomography *IEEE Trans. Bio-Med. Eng.* **59** 383–9

Tang C, You F, Cheng G, Gao D, Fu F, Yang G and Dong X 2008 Correlation between structure and resistivity variations of the live human skull *IEEE Trans. Bio-Med. Eng.* **55** 2286–92

Tang T and Sadleir R J 2011 Quantification of intraventricular hemorrhage with electrical impedance tomography using a spherical model *Physiol. Meas.* **32** 811–21

Tang T, Oh S and Sadleir R 2010 A robust current pattern for the detection of intraventricular hemorrhage in neonates using electrical impedance tomography *Ann. Biomed. Eng.* **38** 2733–47

Tidswell A T, Bagshaw A P, Holder D S, Yerworth R J, Eadie L, Murray S, Morgan L and Bayford R H 2003 A comparison of headnet electrode arrays for electrical impedance tomography of the human head *Physiol. Meas.* **24** 527–44

Tidswell A T, Gibson A, Bayford R H and Holder D S 2001a Validation of a 3D reconstruction algorithm for EIT of human brain function in a realistic head-shaped tank *Physiol. Meas.* **22** 177–85

Tidswell T, Gibson A, Bayford R and Holder D 2001b Three-dimensional electrical impedance tomography of human brain activity *NeuroImage* **13** 283–94

Várady T, Martin R R and Cox J 1997 Reverse engineering of geometric models—an introduction *Comput.-Aided Des.* **29** 255–68

Vauhkonen P, Vauhkonen M, Savolainen T and Kaipio J 1999 Three-dimensional electrical impedance tomography based on the complete electrode model *IEEE Trans. Biomed. Eng.* **46** 1150–60

Wolters C H, Anwander A, Tricoche X, Weinstein D, Koch M A and MacLeod R S 2006 Influence of tissue conductivity anisotropy on EEG/MEG field and return current computation in a realistic head model: a simulation and visualization study using high-resolution finite element modeling *NeuroImage* **30** 813–26